

G2D: From Global to Dense Radiography Representation Learning via Vision-Language Pre-training

Che Liu¹, Cheng Ouyang¹, Sib0 Cheng¹, Anand Shah^{1,2}, Wenjia Bai¹, Rossella Arcucci¹

¹Imperial College London

²Royal Brompton and Harefield Hospital

Abstract

Recently, medical vision-language pre-training (VLP) has reached substantial progress to learn global visual representation from medical images and their paired radiology reports. However, medical imaging tasks in real world usually require finer granularity in visual features. These tasks include visual localization tasks (e.g., semantic segmentation, object detection) and visual grounding task. Yet, current medical VLP methods face challenges in learning these fine-grained features, as they primarily focus on brute-force alignment between image patches and individual text tokens for local visual feature learning, which is suboptimal for downstream dense prediction tasks. In this work, we propose a new VLP framework, named **Global to Dense** level representation learning (G2D) that achieves significantly improved granularity and more accurate grounding for the learned features, compared to existing medical VLP approaches. In particular, G2D learns dense and semantically-grounded image representations via a pseudo segmentation task parallel with the global vision-language alignment. Notably, generating pseudo segmentation targets does not incur extra trainable parameters: they are obtained on the fly during VLP with a parameter-free processor. G2D achieves superior performance across 6 medical imaging tasks and 25 diseases, particularly in semantic segmentation, which necessitates fine-grained, semantically-grounded image features. In this task, G2D surpasses peer models even when fine-tuned with just 1% of the training data, compared to the 100% used by these models. The code will be released upon acceptance.

1. Introduction

In medical image analysis, obtaining precise annotations is both labor-intensive and financially burdensome. Self-supervised learning (SSL) has made significant progress in visual representation learning from images [3, 6], yet single modality SSL may neglect the incorporation of domain-

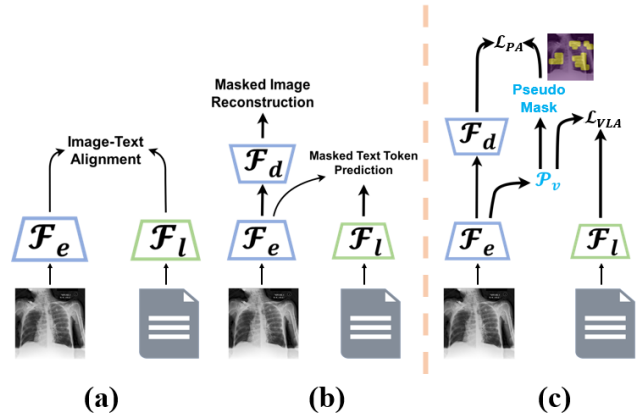


Figure 1. Comparison between other medical VLP approaches and G2D. (a) Alignment-based approaches. (b) Reconstruction-based approaches. (c) Framework of **G2D (ours)**, which combines a pseudo segmentation task and global vision-language alignment to learn dense, semantically-grounded image representations.

specific clinical knowledge. Vision-language pre-training (VLP) has been introduced to address this issue, effectively aligning vision and language content, typically in extensive datasets [18, 25, 38, 42]. It is noteworthy that in standard clinical practices, chest X-ray (CXR) scans are commonly coupled with radiology reports [19]. These reports, even in the absence of diagnostic labels, are rich with clinical domain knowledge. Recognizing the potential of these unannotated CXR image-report pairs, medical VLP has emerged as a pivotal technique [30], achieving remarkable progress in representations learning from such unlabeled datasets. Presently, medical VLP methods can be categorized into two primary streams, as illustrated in Fig 1:

- **Alignment-based Approaches:** These strategies emphasize the semantic alignment between images and reports at different levels [4, 10, 18–20, 35, 38, 42]. For instance, [42] aligns the entirety of an image with a full report, aiming to capture the global visual representation. GLORIA [10] and MGCA [35] are designed for token-level alignment, specifically for fine-grained representation learning.

- **Reconstruction-based Approaches:** These methods [4, 44] primarily concentrate on representation learning by reconstructing masked or inpainted images, as well as masked language modeling.

Despite advancements in medical VLP methods, inherent limitations exist: current techniques align image patches with text tokens in a brute-force manner with contrastive objectives, potentially causing misalignments when tokens (*e.g.*, ‘compatible’ or ‘unremarkable’) lack direct visual counterparts, leading to ambiguous local alignments. Conversely, reconstruction-based strategies ignore the high-level image semantics. They predominantly emphasize recovering the low-level visual information such as intensity and texture, limiting the transferability to diverse downstream tasks such as semantic segmentation that rely on high-level semantics [8, 21, 22]. As a result, both strategies perform suboptimally in dense representation learning due to the gap between the representations learned from the pretext task and those required by downstream tasks. Downstream tasks, such as semantic segmentation and visual grounding, demand granular visual features with high-level semantics. However, the pretext task often risks learning misaligned dense visual features or those with low-level semantics [16, 40].

While various VLP methods are designed to capture dense visual features for photographic imagery, they often struggle to transfer directly to medical images because they depend on a well-trained object detection model [7, 16] or a well-aligned VLP model [23, 43]. Yet, in the medical domain, obtaining such external models is difficult because objects can be defined in various ways (*e.g.*, based on organ regions, pathological tissues, or abnormal regions) within a single medical image. Additionally, unlike in non-medical domain [25], in medical domain, there is a lack of foundational VLP models that are both publicly accessible and are trained on sufficiently large image-text pairs that cover diverse highly specialized medical applications.

In response to the aforementioned challenges, we introduce a novel medical VLP architecture termed G2D. This framework is designed to extract global and dense visual representations from radiography along with their associated radiology reports, with both improved **feature granularity** and enriched **semantic information**. Central to our approach is a unique pretext task named **pseudo segmentation (PS)**, which is guided by a pseudo mask (segmentation target) derived from a meticulously refined and filtered attention map. PS encourages the model to learn dense representations through pixel-level constraints that incorporate high-level semantics, aligning each pixel with pseudo masks derived from features in alignment with radiology reports. This approach, in contrast to traditional methods that align with image patches and text tokens, inherently avoids misalignment bias. Consequently, PS offers

more representative feature learning than VLP methods that focus on low-level semantics through pixel reconstruction pretext tasks. Notably, this task operates concurrently with vision-language alignment, ensuring the VLP framework to be end-to-end, contrasting with the cumbersome two-stage methods [43].

To evaluate the effectiveness of G2D relative to other state-of-the-art (SOTA) approaches, we deploy the pre-trained model across a diverse range of downstream tasks. These tasks span supervised medical image classification, semantic segmentation, object detection, as well as zero-shot image classification and visual grounding. Our experimental results, which cover six public large-scale CXR datasets, confirm G2D’s superior performance over established works. Overall, Our contribution is three-fold:

1. We introduce G2D, the first end-to-end encoder-decoder medical VLP architecture designed to learn visual representations from the global level down to the dense level, supervised by associated radiology reports and a newly proposed pretext task.
2. We design a new pretext task for medical VLP, termed pseudo segmentation. This task is supervised by a pseudo mask as segmentation target, and is designed to narrow the gap between the dense visual representations learned in the pretext task and those required by downstream dense visual tasks. The generation of this mask is performed by a parameter-free processor, in conjunction with an attention map derived from the visual representation that aligns with radiology reports.
3. We conduct comprehensive experiments to validate the efficacy of our proposed G2D framework. This method outperforms all peer approaches across six uni-modal and cross-modal downstream tasks.

2. Related work

Alignment-based Medical VLP Drawing inspiration from [25], aligning images with their corresponding textual descriptions in the latent space has led to notable advancements in VLP. Within the CXR domain, while CONVIRT [42] made an early attempt at employing bidirectional contrastive learning to globally align entire images with their paired reports, there remained room for refinement. GLORIA [10] and MGCA [35] represent advancements in image-report alignment, introducing sophisticated global-local methodologies to the field [10, 35]. These approaches endeavor to establish correspondences between distinct image and text tokens. However, it is crucial to recognize that the granularity of token-level alignment could inadvertently introduce distortions to the medical context, potentially leading to misalignments, as illustrated by [19, 34]. Med-UniC [34] utilizes augmented text in VLP training to cultivate language invariance, with the goal of mitigating linguistic biases from VLP. Meanwhile, MedKLIP [38] and

KAD [41] harness domain-specific knowledge from external annotated datasets to enhance textual information extraction. Notably, these approaches [34, 38, 41] are contingent upon external resources or extra data to optimize cross-modal representation learning, which could potentially constrain their generalizability.

Reconstruction-based Medical VLP Several studies, including [4, 11, 44], have employed reconstruction of image and text tokens as a pretext task within VLP. Specifically, MRM [44] endeavors to reconstruct the original image from a masked version and simultaneously aims to regenerate the original text using both the masked image and text as inputs. Conversely, PRIOR [4] adopts a strategy that focuses on cross-modal representation by reconstructing images and sentences based on complete image and report inputs. An enhancement to the MRM [44] approach is proposed by [11], where token weights are adjusted during the reconstruction phase.

While these methods have demonstrated promising outcomes, the ability of the reconstruction pretext task to capture high-level semantic representations is limited, as shown in [8, 21, 22], and is further challenged by the absence of explicit semantic-related constraints in dense visual representation learning.

3. Methodology

In the G2D framework we propose, the central aim is to concurrently learn global and dense cross-modal representations from CXR images and their corresponding radiology reports. As illustrated in Fig 2, G2D integrates two alignment strategies: the vision-language alignment (VLA) targeting a global perspective, and the pixel alignment (PA) focusing on granular representation through our proposed pixel-level pretext task, termed **pseudo segmentation (PS)**. The details of PS are elaborated upon in Sec 3.2 and 3.3. The construction of the pseudo mask for PS is meticulously achieved through a parameter-free mechanism, ensuring training efficiency. This mechanism operates alongside VLA, enabling G2D to derive dense representations at both encoder and decoder levels during the VLP process. Post VLP, the representations learned from PA prove crucial for visual localization tasks that necessitate a more fine-grained representation over a global one, such as semantic segmentation and object detection. Moreover, the PS pretext task in G2D facilitates a smoother transfer to downstream segmentation tasks, reducing the gap between the dense visual representation learned from the pre-trained encoder-decoder architecture and the needs of downstream dense visual tasks. This contrasts with previous methods [10, 18, 35, 38, 41, 42] that typically transfer only the pre-trained encoder, potentially leading to information gaps and the discrepancy between the pretext and downstream tasks.

3.1. Vision-Language Contrastive Learning

We utilize a dual-encoder image-text contrastive approach following [10, 35, 38, 42]. For VLA, given a training set of N image-text dataset S consisting of pairs (v_i, l_i) , where $v_i \in \mathcal{V}$ is a raw CXR image and $l_i \in \mathcal{L}$ is a text report, $i = 1, 2, 3, \dots, N$. The G2D architecture employs an image encoder $\mathcal{F}_e : \mathcal{V} \mapsto \mathbb{R}^{D_v}$ to encode the raw image into embeddings of dimension D_v , and a text encoder $\mathcal{F}_l : \mathcal{L} \mapsto \mathbb{R}^{D_l}$ to encode the text report into embeddings of dimension D_l . Then dataset in feature-level can be denoted as $\mathbf{S} = \{(\mathbf{v}_1, \mathbf{l}_1), (\mathbf{v}_2, \mathbf{l}_2), \dots, (\mathbf{v}_N, \mathbf{l}_N)\}$, where $\mathbf{v}_i = \mathcal{F}_e(v_i)$ and $\mathbf{l}_i = \mathcal{F}_l(l_i)$.

As depicted in Fig 2, G2D incorporates two concurrent alignment strategies: VLA and PA. For VLA, the model aims to learn global visual representation from paired medical reports by pulling the embeddings of paired image-report samples closer while distancing embeddings of unmatched pairs, under the loss \mathcal{L}_{VLA} . Following the CLIP framework [25], a contrastive learning objective is incorporated to predict the matched pair (v_i, l_i) from $N \times N$ possible image-text pairs while distancing $N^2 - N$ negative pairs. Specifically, two non-linear vision and language projectors \mathcal{P}_v and \mathcal{P}_l are utilized to transform \mathbf{v}_i and \mathbf{l}_i into the same dimension d , where $\hat{\mathbf{v}}_i = \mathcal{P}_v(\mathbf{v}_i)$, $\hat{\mathbf{l}}_i = \mathcal{P}_l(\mathbf{l}_i)$, and $\hat{\mathbf{v}}_i, \hat{\mathbf{l}}_i \in \mathbb{R}^d$. Upon obtaining image feature vectors $[\hat{\mathbf{v}}_i]_{i=1}^N$ and text feature vectors $[\hat{\mathbf{l}}_i]_{i=1}^N$ from a training batch, cosine similarities $s_{i,i}^{v2l} = \hat{\mathbf{v}}_i^\top \hat{\mathbf{l}}_i$ and $s_{i,i}^{l2v} = \hat{\mathbf{l}}_i^\top \hat{\mathbf{v}}_i$ are computed, representing image-text and text-image similarities, respectively. \mathcal{L}_{VLA} is then formulated as:

$$\begin{aligned} \mathcal{L}_{VLA} &= \frac{1}{2K} \sum_{i=1}^N (\mathcal{L}_v^{v2l} + \mathcal{L}_l^{l2v}), \text{ where} \\ \mathcal{L}_v^{v2l} &= -\log \frac{\exp(s_{i,i}^{v2l}/\sigma)}{\sum_{j=1}^K \exp(s_{i,j}^{v2l}/\sigma)}, \\ \mathcal{L}_l^{l2v} &= -\log \frac{\exp(s_{i,i}^{l2v}/\sigma)}{\sum_{j=1}^K \exp(s_{i,j}^{l2v}/\sigma)}. \end{aligned} \quad (1)$$

Here, \mathcal{L}_v^{v2l} and \mathcal{L}_l^{l2v} are image-text and text-image contrastive losses based on InforNCE [32], respectively. σ is the temperature hyper-parameter set to 0.07 in our experiments following [35], $K \in N$ is the batch size.

3.2. Pseudo Segmentation Mask Construction

Attention Aggregation Inspired by CLIP [25], we incorporate an attention pooling mechanism in conjunction with the non-linear projector \mathcal{P}_v to derive attention scores for each pixel embedding. The dense feature map \mathbf{V}_i , sourced from the final convolutional layer before the pooling operation in the image encoder \mathcal{F}_e , is characterized by the dimensions $C \times H \times W$. Here, C denotes the number of channels, while H and W represent the height and width

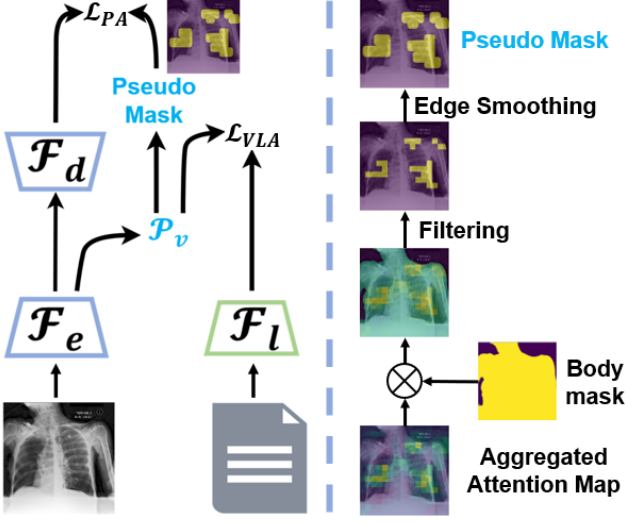


Figure 2. **Left:** Framework of G2D. **Right:** Pipeline for pseudo mask construction.

of the feature maps, respectively. Subsequently, we reshape \mathbf{V}_i into a dimension of $HW \times C$. Consequently, \mathbf{V}_i can be interpreted as a sequence of pixel embeddings, where each token in this sequence represents the embedding of an individual pixel. The length of this sequence is defined by the number of channels, C . A special token, [CLS], is introduced to aggregate all pixel embeddings through multi-head self-attention (MHSA) [25, 33]. This process offers an attention score matrix W_i^h for each pixel embedding, with dimensions $h \times H \times W$. Here, h signifies the attention head number, and $h \in \mathcal{H}$, with \mathcal{H} being the total number of attention heads.

To derive the pseudo mask, we aggregate W_i^h 's across all attention heads to produce \hat{W}_i , as described by:

$$\hat{W}_i = \frac{\sum_{h=1}^{\mathcal{H}} W_i^h}{h} \quad (2)$$

Mask Filtering and Edge Smoothing Upon obtaining the aggregated attention matrix, we resize \hat{W}_i to match the original image's dimensions $H' \times W'$. To remove pseudo mask regions falling at non-body parts, we construct the body mask for each CXR image using a simple histogram-based thresholding approach, following common practice [13, 24]. Subsequently, all attention scores outside the body mask are set to zero. A threshold is then applied to filter out low attention scores in the body mask, transforming \hat{W}_i into a binary mask suitable for PS. This threshold is determined as the 85% percentile of values from \hat{W}_i . Consequently, the mask M_i is formulated as:

$$M_i^{j,k} = \begin{cases} 1 & \text{if } W_i^{j,k} \geq \text{threshold} \\ 0 & \text{otherwise} \end{cases}, \text{ where} \\ j = 1, 2, 3, \dots, H', k = 1, 2, 3, \dots, W' \quad (3)$$

To make the mask boundary appear natural, we employ the Bilateral Filter (BF) [31] to smooth the square-like edges in M_i , resulting in the refined mask \tilde{M}_i . A comprehensive ablation study discussing the threshold and smoothing operations is presented in Sec 4.6.

3.3. Dense Visual Representation Learning through Pseudo Segmentation in VLP

While the global visual representation can be learned via VLA, dense representation often lacks direct alignment. To tackle this limitation, we introduce an image decoder, denoted as \mathcal{F}_d , as shown in Fig 2 left. This decoder takes visual feature \mathbf{V}_i as input and utilizes the pseudo mask \tilde{M}_i as the supervision signal for the PS task. We employ the commonly used soft dice loss and binary cross-entropy loss [13] to optimize this task. This training objective \mathcal{L}_{PA} can be expressed as:

$$\mathcal{L}_{PA} = \frac{1}{2}(\mathcal{L}_{Dice} + \mathcal{L}_{BCE}), \text{ where} \\ \mathcal{L}_{Dice} = \sum_{i=1}^K \sum_{j=1}^{H'} \sum_{k=1}^{W'} \left(1 - \frac{2 \times (\tilde{M}'_{i,j,k} \odot \tilde{M}_{i,j,k})}{\tilde{M}'_{i,j,k} + \tilde{M}_{i,j,k}} \right), \\ \mathcal{L}_{BCE} = \sum_{i=1}^K \sum_{j=1}^{H'} \sum_{k=1}^{W'} -\tilde{M}_{i,j,k} \log(\tilde{M}'_{i,j,k}), \\ - \sum_{i=1}^K \sum_{j=1}^{H'} \sum_{k=1}^{W'} (1 - \tilde{M}_{i,j,k}) \log(1 - \tilde{M}'_{i,j,k}), \text{ and} \\ \tilde{M}'_i = \mathcal{F}_d(\mathbf{V}_i) \quad (4)$$

Subsequently, the total loss for the G2D framework is the summation of the VLA loss (Eq. 1) and the PA loss (Eq. 4):

$$\mathcal{L}_{total} = \mathcal{L}_{VLA} + \mathcal{L}_{PA} \quad (5)$$

4. Experiment and Analysis

In this section, we primarily compare our approach with SOTA medical VLP techniques. For implementation details and dataset splitting, please refer to the appendix.

4.1. Pretraining Dataset and Configuration

We utilize the MIMIC-CXR dataset [14, 15] which, after preprocessing based on established protocols, provides 213,384 image-text pairs for pre-training [35, 38]. For the VLP phase, we employ a standard ResNet-50 as our vision encoder \mathcal{F}_e and adopt the decoder part from a standard U-Net as our vision decoder \mathcal{F}_d . We adopt ClinicalBERT [1] as our text encoder, consistent with the configurations in [38, 41]. In alignment with [10, 35], G2D is pre-trained for 50 epochs across 16 A100 GPUs, each accommodating

a batch size of 128. The AdamW optimizer is employed with a learning rate set to 2×10^{-4} and a weight decay of 1×10^{-8} . Additionally, a linear warm-up and cosine annealing scheduler are also incorporated in the training process.

4.2. Downstream Task Datasets and Configurations

In our downstream tasks, our focus is on evaluating the efficacy of G2D in visual localization, vision-language understanding, and visual recognition tasks. Specifically, we examine the capability and transferability of the learned cross-modal representations by subjecting them to evaluations across six distinct medical imaging tasks, covering a spectrum of 25 different diseases.

4.2.1 Visual Localization Tasks

Medical Image Semantic Segmentation This task utilizes the RSNA [28] and SIIM [29] datasets, following pre-processing guidelines established in [10, 35]. We adopt U-Net [27] fine-tuning configurations following [10, 35]. The encoders from the pre-trained vision backbone are kept frozen, while only the decoders’ parameters are updated during fine-tuning. Performance is assessed using Dice scores, following the protocol described in [10, 35].

Medical Image Object Detection This task is executed on RSNA [28] and Object-CXR [9] datasets, adhering to pre-processing from [35]. We employ YOLOv3 [26] for detection, using our pre-trained encoder as the visual backbone and updating only the detection head during fine-tuning. Evaluation relies on Mean Average Precision (mAP) with IOU thresholds 0.4~0.75. The setup for this task is in accordance with the pipelines provided in [35].

4.2.2 Vision-Language Understanding Tasks

Zero-shot Medical Image Visual Grounding In accordance with the methodology outlined in [38], this task is conducted on the RSNA [28] and SIIM [29] datasets. We employ CXR images as input and utilize the corresponding dense label maps as ground truth. The official data split and evaluation metrics, as specified by [38], are adopted. These metrics include Recall, IoU, and Dice score.

Zero-shot Medical Image Classification In compliance with the guidelines set forth in [38, 41], we conduct this task on the RSNA [28] and SIIM datasets [29]. Utilizing the official test set split ensures a fair comparison with [38]. Our prompts are designed in accordance with [30], with positive and negative prompts formatted as ‘*disease*’ and ‘No *disease*’, respectively, where *disease* represents the category name. We report results using the macro average of AUC, F1, and ACC scores across all diseases. The image pre-processing involves resizing to 256×256 , center-cropping to 224×224 , and normalizing pixel values to the $[0, 1]$ range, in accordance with [38, 41]. Both image and text prompts

are encoded to generate respective embeddings, and classification is evaluated through the cosine similarity between these embeddings for each class-specific prompt.

4.2.3 Visual Recognition Tasks

Medical Image Fine-tuned Classification In alignment with [38, 41], we use the CXR14 dataset [37], comprising 112,120 frontal-view X-rays from 30,805 patients, annotated for 14 diseases. We adhere to the official split for consistent evaluation. During fine-tuning, all model parameters are updated, including the pre-trained encoder and linear classifier. CXR images are resized to 256×256 [41]. Optimization uses the AdamW optimizer with a learning rate of 1×10^{-4} and a batch size of 64 for 50 epochs. Evaluation is based on the AUC score, adhering to the protocol outlined in [10, 35, 44].

Medical Image Linear Classification In strict accordance with the configuration from [10, 35, 42], this task is rigorously conducted on the CheXpert [12], RSNA [28], and COVIDx [36] datasets. We only update a randomly initialized linear classification layer, while the pre-trained vision backbone remains frozen. For fair evaluation, we employ AUC scores on CheXpert and RSNA, along with accuracy metrics on COVIDx, as mentioned in [10, 35].

Excluding zero-shot image classification and visual grounding, we rigorously fine-tune on 1%, 10%, 100% of the training data for all downstream tasks. Detailed settings, including implementation and data splits, are concisely outlined in the appendix.

4.3. Performance on Visual Localization Tasks

In Tab 1, following [16, 40], we evaluate G2D alongside other SOTA approaches on two pivotal visual localization tasks: semantic segmentation and object detection. The aim is to assess the efficacy of the dense visual features learned.

Initially, we transfer only the encoder weights from the pre-trained G2D for the segmentation task, adhering to the protocols of [10, 35, 38]. In this setup, our approach consistently achieves the highest performance across all data fractions for both SIIM [29] and RSNA datasets [28]. To assess the impact of the visual decoder pre-trained with the PS pretext task, we transfer the weights of both the encoder and decoder from G2D for the segmentation task, resulting in striking outcomes. Remarkably, with just 1% of training data, G2D surpasses the performance of all peer methods, even those fine-tuned with a full 100% of training data. This observation underlines the fact that the pixel-level pretext task, PS, significantly amplifies the quality of local visual features derived from VLP, proving especially advantageous for the dense prediction task.

In object detection, our method consistently outperforms all baselines across every data fraction for both RSNA and

Method	Semantic Segmentation (Dice)						Object Detection (mAP)					
	SIIM			RSNA			RSNA			Object CXR		
	1%	10%	100%	1%	10%	100%	1%	10%	100%	1%	10%	100%
Random Init	9.0	28.6	54.3	6.9	10.6	18.5	1.0	4.0	8.9	-	0.5	4.4
ImageNet Init	10.2	35.5	63.5	34.8	39.9	64.0	3.6	8.0	15.7	-	2.9	8.3
ConVIRT [42]	25.0	43.2	59.9	55.0	67.4	67.5	8.2	15.6	17.9	-	8.6	15.9
GLoRA [10]	35.8	46.9	63.4	59.3	67.5	67.8	9.8	14.8	18.8	-	10.6	15.6
GLoRIA-MIMIC [10]	37.4	57.1	64.0	60.3	68.7	68.3	11.6	16.1	24.8	-	8.90	16.6
MGCA [35]	49.7	59.3	64.2	63.0	68.3	69.8	12.9	16.8	24.9	-	12.1	19.2
M-FLAG [18]	52.5	61.2	64.8	64.6	69.7	70.5	13.7	17.5	25.4	-	12.4	19.3
MedKLIP* [38]	50.2	60.8	63.9	66.2	69.4	71.9	8.9	16.3	24.5	-	7.1	11.6
Ours (encoder)	62.6	63.1	66.8	70.9	72.6	75.1	15.9	21.7	27.2	3.8	13.1	20.4
Ours (encoder-decoder)	65.6	66.9	68.4	72.8	73.4	76.9	/	/	/	/	/	/

Table 1. Results of semantic segmentation on SIIM and RSNA datasets and object detection on RSNA and Object-CXR datasets. The best results for each setting are highlighted in bold, and the ‘-’ denotes mAP values smaller than 1%. Methods with * leverage disease-level annotations. ‘/’ indicates that the object detection task cannot be deployed with an encoder-decoder architecture model.

Object-CXR datasets [9, 28]. Notably, G2D achieves a 3.8% mAP on the Object-CXR dataset with just 1% of the data for fine-tuning, a significant leap from other methods that scarcely reach a 1% mAP.

These results highlight the efficacy of our proposed model, G2D, and the pretext task, PS, especially in semantic segmentation tasks that rely on dense features. PS not only enables G2D to learn visual representations in the encoder-decoder structure but also reduces the gap between pre-training and downstream tasks. By enhancing the encoder’s ability to capture global and dense features simultaneously, PS surpasses all SOTA approaches, proving particularly advantageous for object detection tasks that heavily rely on dense features [17].

4.4. Performance on Vision-Language Understanding

In Tab 2, we evaluate the efficacy of G2D on vision-language understanding tasks, zero-shot visual grounding and zero-shot image classification. For the zero-shot visual grounding task, our proposed method outperforms peer approaches. Specifically, on the SIIM dataset [29], it achieves a leading Dice score of 5.1. This dominance persists in the RSNA dataset [28], where our method reaches a Dice score of 47.7, surpassing other SOTA approaches. When examining zero-shot image classification, our method again shows its superiority across the AUC, F1, and ACC metrics on both the RSNA [28] and SIIM datasets [29]. Such consistent and superior outcomes underscore the adaptability and effectiveness of G2D in handling vision-language understanding tasks, indicating that integrating PS into G2D can enhance not only uni-modal but also cross-modal tasks.

4.5. Performance on Visual Recognition Tasks

In our final assessment focused on visual recognition, Tab 3 demonstrates our method’s consistent supremacy on the CXR14 dataset [37] for fine-tuned disease classification across 1%, 10%, and 100% training data. Similarly, Tab

Zero-shot Visual Grounding						
Methods	SIIM			RSNA		
	Recall	IoU	Dice	Recall	IoU	Dice
GLoRIA [10]	23.8	1.2	2.1	83.3	21.8	34.7
BioViL [2]	19.6	1.7	2.6	85.2	30.3	43.9
MedKLIP* [38]	35.6	2.1	4.0	86.6	31.7	46.5
Ours	37.7	3.9	5.1	88.4	33.5	47.7

(a) Results of zero-shot visual grounding task.

Zero-shot Image Classification						
	RSNA			SIIM		
	AUC	F1	ACC	AUC	F1	ACC
ConVIRT [42]	80.4	58.4	76.1	64.3	43.3	57.0
GLoRIA [10]	71.5	49.0	71.3	53.4	38.2	40.5
BioViL [2]	82.8	58.3	76.7	70.8	48.6	69.1
CheXzero* [38]	85.8	62.1	79.4	68.8	47.0	54.7
MedKLIP* [38]	86.9	63.4	80.0	89.2	68.3	84.3
Ours	87.6	64.8	81.5	89.7	69.3	85.4

(b) Results of zero-shot image classification task.

Table 2. Comparison between G2D (ours) and various other medical VLP methods in vision-language understanding tasks, with the best results emphasized in bold. Methods marked with * utilize extra annotated data during pre-training.

4 underscores that G2D achieves the highest performance on the CheXpert, RSNA, and COVIDx datasets [12, 28, 36] for linear evaluation across all training data ratio. Notably, G2D consistently outperforms even those methods like MedKLIP and KAD [39] that leverage additional disease-level annotations during pre-training stage. This demonstrates G2D’s representative visual features, suggesting that enhancing dense representation learning via PS can also improve results in tasks primarily anchored on global representation.

4.6. Ablation Studies

Pseudo Segmentation vs. Reconstruction In Tab 5a, we evaluate the impact of our proposed PS pretext task in

Data fraction	Method	Mean	Atelectasis	Cardiomegaly	Effusion	Infiltration	Mass	Nodule	Pneumonia	Pneumothorax	Consolidation	Edema	Emphysema	Fibrosis	Pleural Thickening	Hernia
1%	Random Init	58.1	55.7	57.7	63.6	61.6	55.0	60.2	57.1	58.2	60.8	63.3	53.4	63.7	56.8	46.0
	ImageNet Init	63.5	66.2	64.2	72.1	57.0	59.0	58.5	60.0	62.6	62.4	66.8	61.5	70.7	63.1	64.5
	ConVIRT [42]	64.9	66.0	78.2	78.9	61.1	59.6	65.5	60.8	68.8	65.7	60.7	65.8	68.0	62.7	46.6
	GLoRIA [10]	59.7	59.7	56.7	74.1	64.6	55.9	55.7	61.1	60.7	66.5	66.9	55.0	55.8	59.2	43.6
	BioViL [2]	57.9	55.5	56.4	72.2	65.0	56.7	54.6	62.6	56.0	65.7	68.1	51.6	51.3	59.2	36.0
	MedKLIP* [38]	60.9	65.5	59.0	74.5	64.3	55.0	61.1	60.9	59.9	65.9	68.2	53.5	64.8	59.3	40.0
	KAD* [41]	78.7	77.0	88.2	82.9	69.2	75.1	69.7	73.5	86.1	72.7	81.3	89.3	74.3	69.2	93.8
	Ours	79.1	78.1	88.3	83.1	70.2	75.4	69.7	74.0	86.5	72.9	81.6	90.2	74.4	69.5	94.1
10%	Random Init	69.1	68.2	76.6	74.6	67.4	62.3	58.0	63.6	72.8	67.8	78.0	64.7	71.5	65.3	77.1
	ImageNet Init	72.6	70.9	79.8	76.9	68.4	69.3	65.6	63.0	79.3	67.1	76.7	74.9	72.9	71.1	81.0
	ConVIRT [42]	77.1	74.0	84.3	81.1	69.3	74.8	70.0	67.1	82.8	70.1	81.4	87.1	76.7	71.9	89.3
	GLoRIA [10]	74.3	72.1	80.8	80.0	68.7	73.3	67.5	65.8	77.9	67.6	79.7	79.9	78.7	69.3	78.7
	BioViL [2]	72.7	70.3	78.5	79.0	66.6	71.8	67.1	66.5	76.7	68.4	79.9	76.1	74.8	65.3	76.3
	MedKLIP* [38]	74.8	72.9	80.2	79.3	69.8	71.9	68.1	66.6	79.6	69.6	81.1	79.5	75.6	71.3	81.9
	KAD* [41]	80.7	77.6	88.9	83.3	71.8	78.3	71.9	73.7	87.2	75.0	83.3	90.3	80.7	72.3	95.3
	Ours	81.1	78.4	89.3	83.7	72.2	78.8	72.3	74.1	87.8	75.3	84.0	90.4	80.8	72.5	95.4
100%	Random Init	79.0	75.0	87.9	81.5	69.1	79.8	72.6	70.3	82.6	73.1	83.9	83.5	80.7	75.4	90.3
	ImageNet Init	80.4	76.3	86.7	82.3	69.3	82.3	76.3	71.9	84.0	73.7	84.2	89.3	81.9	77.0	89.9
	ConVIRT [42]	80.8	77.1	86.7	82.5	70.3	81.8	76.1	72.2	85.7	74.7	85.4	90.1	80.9	77.1	90.9
	GLoRIA [10]	80.0	76.0	85.5	81.8	70.0	81.4	74.9	71.5	82.8	73.9	83.2	88.7	81.3	76.7	92.1
	BioViL [2]	80.0	76.5	87.1	82.4	69.7	81.9	75.2	71.0	84.5	74.2	84.2	87.1	82.1	75.9	88.8
	MedKLIP* [38]	80.1	76.4	84.9	82.3	69.7	82.0	74.7	71.2	83.9	75.1	84.8	87.9	81.7	77.7	89.2
	KAD* [41]	82.5	78.5	89.7	84.0	71.3	83.6	77.1	74.0	87.4	75.3	86.0	91.6	82.9	77.8	96.1
	Ours	83.1	79.9	90.2	84.5	71.8	84.2	78.0	74.2	87.7	75.6	86.9	92.0	83.1	78.2	96.5

Table 3. Evaluation of different medical VLP methods for image classification fine-tuning on the CXR14 dataset. All metrics are presented as AUC scores, with the mean metric being macro-averaged. Best performances are highlighted in bold. Methods with * use extra annotated data for pre-training.

Method	CheXpert (AUC)			RSNA (AUC)			COVIDx (ACC)		
	1%	10%	100%	1%	10%	100%	1%	10%	100%
Random Init	56.1	62.6	65.7	58.9	69.4	74.1	50.5	60.3	70.0
ImageNet Init	74.4	79.7	81.4	74.9	74.5	76.3	64.8	78.8	86.3
ConVIRT [42]	85.9	86.8	87.3	77.4	80.1	81.3	72.5	82.5	92.0
GLoRIA [10]	86.6	87.8	88.1	86.1	88.0	88.6	67.3	77.8	89.0
GLoRIA-MIMIC [10]	87.1	88.7	88.0	87.0	89.4	90.2	66.5	80.5	88.8
MGCA [35]	87.6	88.0	88.2	88.6	89.1	89.9	72.0	83.5	90.5
MRM [44]	88.5	88.5	88.7	91.3	92.7	93.3	66.9	79.3	90.8
MedKLIP* [38]	86.2	86.5	87.7	87.3	88.0	89.3	74.5	85.2	90.3
Ours	89.7	90.4	91.1	92.2	92.9	93.6	76.6	88.2	93.4

Table 4. Linear classification results for CheXpert, RSNA, and COVIDx datasets with 1%, 10%, and 100% training data. The best results are highlighted in bold. Methods with * leverage disease-level annotations for pre-training.

comparison to pixel reconstruction and models without a decoder-level constraint. The model pre-trained with PS outperforms the other two approaches across all three downstream tasks, particularly in semantic segmentation. While the model pre-trained with a pixel reconstruction constraint exhibit improved performance compared to unconstrained variants, such models are still outperformed by the model with the PS constraint. These results underscore the effectiveness of decoder-level pretext tasks and suggest that an emphasis on high-level semantics, derived from PS, is more beneficial than focusing on the low-level semantics from pixel reconstruction. The PS potentially reduces the dis-

parity between features learned through VLP and those required by downstream semantic segmentation tasks. It also enables the model to acquire more representative features that are beneficial for various tasks.

Criteria of Pseudo Mask Construction As shown in Tab 5b, performance varies with different thresholds, with the 85% quantile threshold proving most effective across all three downstream tasks. Despite employing the Gaussian Mixture Model (GMM) for pseudo mask creation, as suggested by [5], its performance is still surpassed by the 85% quantile approach. This indicates that the original attention map might contain noise, and a higher threshold is benefi-

Decoder Loss	SIIM Dice	RSNA mAP	CXR14 AUC
None	49.2±1.5	11.7±1.2	77.1±1.5
Reconstruction	53.4±1.3	13.0±0.9	77.3±2.1
Pseudo Seg (Ours)	65.6±1.7	15.9±0.8	79.1±1.2

(a) Optimization targets for the decoder. The term ‘None’ indicates Encoder-Only visual backbones.

Method	SIIM Dice	RSNA mAP	CXR14 AUC
w Aggregation	65.6±1.7	15.9±0.8	79.1±1.2
w/o Aggregation	62.1±2.2	13.5±1.7	77.5±2.3

(d) Ablation of multi-head attention maps aggregation.

Threshold	SIIM Dice	RSNA mAP	CXR14 AUC
85% quantile	65.6±1.7	15.9±0.8	79.1±1.2
75% quantile	63.0±2.1	14.1±1.2	78.3±2.0
median	58.8±1.6	12.5±2.3	75.6±1.1
GMM [5]	59.2±1.5	12.9±1.4	75.2±1.9

(b) Criteria for constructing pseudo segmentation masks threshold.

Heads	SIIM Dice	RSNA mAP	CXR14 AUC
1	63.4±2.0	14.2±1.4	78.2±1.0
2	64.7±1.6	15.1±2.3	78.8±1.5
3	65.6±1.7	15.9±0.8	79.1±1.2
4	65.3±1.6	15.4±0.9	78.7±1.9

(e) Number of attention heads.

Num of Dim	SIIM Dice	RSNA mAP	CXR14 AUC
128	65.6±1.7	15.9±0.8	79.1±1.2
256	64.9±1.9	16.1±1.1	78.3±1.5
512	64.6±1.2	15.7±1.0	78.0±1.3

(c) Ablation of the number of dimensions of projectors.

	SIIM Dice	RSNA mAP	CXR14 AUC
w/o body mask	63.4±1.5	15.3±2.1	78.4±1.6
w/o edge smoothing	64.1±1.2	15.2±1.7	78.5±2.2
w both (Ours)	65.6±1.7	15.9±0.8	79.1±1.2

(f) Refinement of Pseudo Segmentation Masks

Table 5. Results of various ablation experiments. The best results are bolded.

cial for generating more effective pseudo masks.

Furthermore, Tab 5d highlights the importance of aggregating multi-head attention maps for mask construction. Given the absence of explicit semantic supervision in the PS pretext task, not aggregating these maps leads to the creation of multiple pseudo masks. This excess of masks introduce ambiguous/conflicting training objectives for VLP.

Impact of Mask Refinement Refinement of the pseudo masks affects the model’s efficacy, as shown in Tab 5f. Performance tends to decrease when either the body mask is omitted or edge smoothing is not applied. However, integrating both these strategies, as we implement in G2D, yields optimal results. This underscores the vital role of pseudo mask refinement in enhancing model performance.

Hyperparameters in VLP VLP performance is sensitive to hyperparameter choices, particularly the number of attention heads and projector dimensionality. Performance improves with more attention heads, peaking at 3 heads before declining slightly at 4 (Tab 5e). Optimal segmentation and classification results occur with 128-dimensional projectors; while 256 dimensions slightly benefit object detection, they lower performance in other tasks (Tab 5c). Projectors of 512 dimensions show no further gains. Hence, we select 3 attention heads and 128-dimensional projectors for an optimal balance of complexity and effectiveness.

4.7. Pseudo Mask Visualization

We visualize the aggregated attention map, pseudo mask, and paired medical reports in Fig 3. Intriguingly, without human annotations, both the attention map and pseudo mask successfully capture image regions corresponding to various report words. Although the pseudo masks don’t perfectly capture every region mentioned in the text, they still manage to capture parts of the image regions related to words, as indicated by the red and blue arrows in Fig 3. This suggests that the supervision signal for the PS pretext task is enriched by the clinical knowledge and high-level

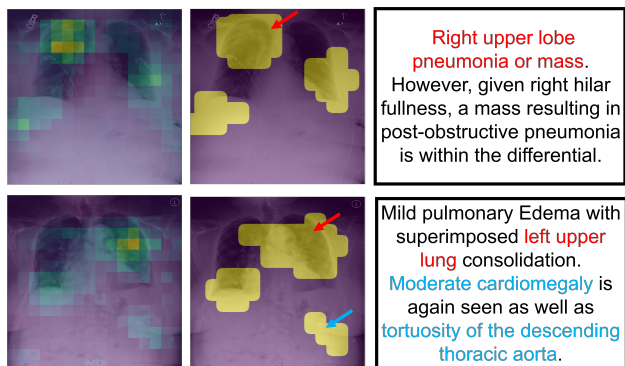


Figure 3. Pseudo Mask Visualization. **Left:** Aggregated attention map. **Middle:** Constructed pseudo mask for the pseudo segmentation task. **Red** and **blue** arrows point to areas related to specific text descriptions. **Right:** Corresponding radiology report. Red and blue text emphasize regions represented in the pseudo mask.

semantics, which explain why the performance with PS is superior to that of the pixel reconstruction pretext task.

5. Conclusion

In this work, we introduce G2D, a novel medical VLP framework designed to learn both global and dense level representations using clinical reports as a supervisory signal. We also propose a new pseudo segmentation pretext task, which compels the model to predict a pseudo mask derived from a refined attention map, thereby capturing dense level visual features during VLP. Remarkably, our model, when pre-trained with this proposed pretext task, achieves superior performance across six varied medical imaging tasks, especially in semantic segmentation. Specifically, on the SIIM [29] dataset, G2D, when fine-tuned with only 1% of the training data, outperforms other medical VLP approaches that utilize the full 100% training set. We hope G2D will inspire further exploration in the realm of pretext tasks for medical VLP.

References

- [1] Emily Alsentzer, John R Murphy, Willie Boag, Wei-Hung Weng, Di Jin, Tristan Naumann, and Matthew McDermott. Publicly available clinical bert embeddings. *arXiv preprint arXiv:1904.03323*, 2019. 4
- [2] Benedikt Boecking, Naoto Usuyama, Shruthi Bannur, Daniel C Castro, Anton Schwaighofer, Stephanie Hyland, Maria Wetscherek, Tristan Naumann, Aditya Nori, Javier Alvarez-Valle, et al. Making the most of text semantics to improve biomedical vision–language processing. In *European conference on computer vision*, pages 1–21. Springer, 2022. 6, 7
- [3] Junyi Chai, Hao Zeng, Anming Li, and Eric WT Ngai. Deep learning in computer vision: A critical review of emerging techniques and application scenarios. *Machine Learning with Applications*, 6:100134, 2021. 1
- [4] Pujin Cheng, Li Lin, Junyan Lyu, Yijin Huang, Wenhan Luo, and Xiaoying Tang. Prior: Prototype representation joint learning from medical images and reports. *arXiv preprint arXiv:2307.12577*, 2023. 1, 2, 3
- [5] Mischa Dombrowski, Hadrien Reynaud, Matthew Baugh, and Bernhard Kainz. Foreground-background separation through concept distillation from generative image foundation models. In *Proceedings of the IEEE/CVF International Conference on Computer Vision*, pages 988–998, 2023. 7, 8
- [6] Andre Esteva, Katherine Chou, Serena Yeung, Nikhil Naik, Ali Madani, Ali Mottaghi, Yun Liu, Eric Topol, Jeff Dean, and Richard Socher. Deep learning-enabled medical computer vision. *NPJ digital medicine*, 4(1):1–9, 2021. 1
- [7] Yuting Gao, Jinfeng Liu, Zihan Xu, Jun Zhang, Ke Li, Rongrong Ji, and Chunhua Shen. Pyramidclip: Hierarchical feature alignment for vision-language model pretraining. *Advances in neural information processing systems*, 35:35959–35970, 2022. 2
- [8] Kaiming He, Xinlei Chen, Saining Xie, Yanghao Li, Piotr Dollár, and Ross Girshick. Masked autoencoders are scalable vision learners. In *Proceedings of the IEEE/CVF Conference on Computer Vision and Pattern Recognition*, pages 16000–16009, 2022. 2, 3
- [9] J Healthcare. Object-cxr-automatic detection of foreign objects on chest x-rays, 2020. 5, 6
- [10] Shih-Cheng Huang, Liyue Shen, Matthew P Lungren, and Serena Yeung. Gloria: A multimodal global-local representation learning framework for label-efficient medical image recognition. In *Proceedings of the IEEE/CVF International Conference on Computer Vision*, pages 3942–3951, 2021. 1, 2, 3, 4, 5, 6, 7
- [11] Weijian Huang, Hongyu Zhou, Cheng Li, Hao Yang, Jiarun Liu, and Shanshan Wang. Enhancing representation in radiography-reports foundation model: A granular alignment algorithm using masked contrastive learning. *arXiv preprint arXiv:2309.05904*, 2023. 3
- [12] Jeremy Irvin, Pranav Rajpurkar, Michael Ko, Yifan Yu, Silvana Ciurea-Ilcus, Chris Chute, Henrik Marklund, Behzad Haghgoo, Robyn Ball, Katie Shpanskaya, et al. Chexpert: A large chest radiograph dataset with uncertainty labels and expert comparison. In *Proceedings of the AAAI conference on artificial intelligence*, pages 590–597, 2019. 5, 6
- [13] Fabian Isensee, Paul F Jaeger, Simon AA Kohl, Jens Petersen, and Klaus H Maier-Hein. nnu-net: a self-configuring method for deep learning-based biomedical image segmentation. *Nature methods*, 18(2):203–211, 2021. 4
- [14] Alistair EW Johnson, Tom J Pollard, Nathaniel R Greenbaum, Matthew P Lungren, Chih-ying Deng, Yifan Peng, Zhiyong Lu, Roger G Mark, Seth J Berkowitz, and Steven Horng. Mimic-cxr-jpg, a large publicly available database of labeled chest radiographs. *arXiv preprint arXiv:1901.07042*, 2019. 4
- [15] Alistair EW Johnson, Tom J Pollard, Nathaniel R Greenbaum, Matthew P Lungren, Chih-ying Deng, Yifan Peng, Zhiyong Lu, Roger G Mark, Seth J Berkowitz, and Steven Horng. Mimic-cxr-jpg, a large publicly available database of labeled chest radiographs. *arXiv preprint arXiv:1901.07042*, 2019. 4
- [16] Liunian Harold Li, Pengchuan Zhang, Haotian Zhang, Jianwei Yang, Chunyuan Li, Yiwu Zhong, Lijuan Wang, Lu Yuan, Lei Zhang, Jenq-Neng Hwang, et al. Grounded language-image pre-training. In *Proceedings of the IEEE/CVF Conference on Computer Vision and Pattern Recognition*, pages 10965–10975, 2022. 2, 5
- [17] Tsung-Yi Lin, Piotr Dollár, Ross Girshick, Kaiming He, Bharath Hariharan, and Serge Belongie. Feature pyramid networks for object detection. In *Proceedings of the IEEE conference on computer vision and pattern recognition*, pages 2117–2125, 2017. 6
- [18] Che Liu, Sibao Cheng, Chen Chen, Mengyun Qiao, Weitong Zhang, Anand Shah, Wenjia Bai, and Rossella Arcucci. M-flag: Medical vision-language pre-training with frozen language models and latent space geometry optimization. In *International Conference on Medical Image Computing and Computer-Assisted Intervention*, pages 637–647. Springer, 2023. 1, 3, 6
- [19] Che Liu, Sibao Cheng, Miaoqing Shi, Anand Shah, Wenjia Bai, and Rossella Arcucci. Imitate: Clinical prior guided hierarchical vision-language pre-training. *arXiv preprint arXiv:2310.07355*, 2023. 1, 2
- [20] Che Liu, Anand Shah, Wenjia Bai, and Rossella Arcucci. Utilizing synthetic data for medical vision-language pre-training: Bypassing the need for real images. *arXiv preprint arXiv:2310.07027*, 2023. 1
- [21] Yuan Liu, Songyang Zhang, Jiacheng Chen, Kai Chen, and Dahua Lin. Pixmim: Rethinking pixel reconstruction in masked image modeling. *arXiv preprint arXiv:2303.02416*, 2023. 2, 3
- [22] Yuan Liu, Songyang Zhang, Jiacheng Chen, Zhaohui Yu, Kai Chen, and Dahua Lin. Improving pixel-based mim by reducing wasted modeling capability. In *Proceedings of the IEEE/CVF International Conference on Computer Vision*, pages 5361–5372, 2023. 2, 3
- [23] Huaishao Luo, Junwei Bao, Youzheng Wu, Xiaodong He, and Tianrui Li. Segclip: Patch aggregation with learnable centers for open-vocabulary semantic segmentation. In *International Conference on Machine Learning*, pages 23033–23044. PMLR, 2023. 2

- [24] Cheng Ouyang, Carlo Biffi, Chen Chen, Turkay Kart, Huaqi Qiu, and Daniel Rueckert. Self-supervision with superpixels: Training few-shot medical image segmentation without annotation. In *Computer Vision–ECCV 2020: 16th European Conference, Glasgow, UK, August 23–28, 2020, Proceedings, Part XXIX 16*, pages 762–780. Springer, 2020. [4](#)
- [25] Alec Radford, Jong Wook Kim, Chris Hallacy, Aditya Ramesh, Gabriel Goh, Sandhini Agarwal, Girish Sastry, Amanda Askell, Pamela Mishkin, Jack Clark, et al. Learning transferable visual models from natural language supervision. In *International Conference on Machine Learning*, pages 8748–8763. PMLR, 2021. [1](#), [2](#), [3](#), [4](#)
- [26] Joseph Redmon and Ali Farhadi. Yolov3: An incremental improvement. *arXiv preprint arXiv:1804.02767*, 2018. [5](#)
- [27] Olaf Ronneberger, Philipp Fischer, and Thomas Brox. U-net: Convolutional networks for biomedical image segmentation. In *Medical Image Computing and Computer-Assisted Intervention–MICCAI 2015: 18th International Conference, Munich, Germany, October 5-9, 2015, Proceedings, Part III 18*, pages 234–241. Springer, 2015. [5](#)
- [28] George Shih, Carol C Wu, Safwan S Halabi, Marc D Kohli, Luciano M Prevedello, Tessa S Cook, Arjun Sharma, Judith K Amorosa, Veronica Arteaga, Maya Galperin-Aizenberg, et al. Augmenting the national institutes of health chest radiograph dataset with expert annotations of possible pneumonia. *Radiology: Artificial Intelligence*, 1(1): e180041, 2019. [5](#), [6](#)
- [29] CIIP Steven G. Langer, PhD and MS George Shih, MD. Siim-acr pneumothorax segmentation. 2019. [5](#), [6](#), [8](#)
- [30] Ekin Tiu, Ellie Talius, Pujan Patel, Curtis P Langlotz, Andrew Y Ng, and Pranav Rajpurkar. Expert-level detection of pathologies from unannotated chest x-ray images via self-supervised learning. *Nature Biomedical Engineering*, pages 1–8, 2022. [1](#), [5](#)
- [31] Carlo Tomasi and Roberto Manduchi. Bilateral filtering for gray and color images. In *Sixth international conference on computer vision (IEEE Cat. No. 98CH36271)*, pages 839–846. IEEE, 1998. [4](#)
- [32] Aäron van den Oord, Yazhe Li, and Oriol Vinyals. Representation learning with contrastive predictive coding. *ArXiv*, abs/1807.03748, 2018. [3](#)
- [33] Ashish Vaswani, Noam Shazeer, Niki Parmar, Jakob Uszkoreit, Llion Jones, Aidan N Gomez, Łukasz Kaiser, and Illia Polosukhin. Attention is all you need. *Advances in neural information processing systems*, 30, 2017. [4](#)
- [34] Zhongwei Wan, Che Liu, Mi Zhang, Jie Fu, Benyou Wang, Sibio Cheng, Lei Ma, César Quilodrán-Casas, and Rossella Arcucci. Med-unic: Unifying cross-lingual medical vision-language pre-training by diminishing bias. *arXiv preprint arXiv:2305.19894*, 2023. [2](#), [3](#)
- [35] Fuying Wang, Yuyin Zhou, Shujun Wang, Varut Vardhanabhuti, and Lequan Yu. Multi-granularity cross-modal alignment for generalized medical visual representation learning. *arXiv preprint arXiv:2210.06044*, 2022. [1](#), [2](#), [3](#), [4](#), [5](#), [6](#), [7](#)
- [36] Linda Wang, Zhong Qiu Lin, and Alexander Wong. Covidnet: A tailored deep convolutional neural network design for detection of covid-19 cases from chest x-ray images. *Scientific reports*, 10(1):1–12, 2020. [5](#), [6](#)
- [37] Xiaosong Wang, Yifan Peng, Le Lu, Zhiyong Lu, Mohammadhadi Bagheri, and Ronald M Summers. Chestx-ray8: Hospital-scale chest x-ray database and benchmarks on weakly-supervised classification and localization of common thorax diseases. In *Proceedings of the IEEE conference on computer vision and pattern recognition*, pages 2097–2106, 2017. [5](#), [6](#)
- [38] Chaoyi Wu, Xiaoman Zhang, Ya Zhang, Yanfeng Wang, and Weidi Xie. Medklip: Medical knowledge enhanced language-image pre-training. *medRxiv*, pages 2023–01, 2023. [1](#), [2](#), [3](#), [4](#), [5](#), [6](#), [7](#)
- [39] Chaoyi Wu, Xiaoman Zhang, Ya Zhang, Yanfeng Wang, and Weidi Xie. Medklip: Medical knowledge enhanced language-image pre-training. *medRxiv*, pages 2023–01, 2023. [6](#)
- [40] Haotian Zhang, Pengchuan Zhang, Xiaowei Hu, Yen-Chun Chen, Liunian Li, Xiyang Dai, Lijuan Wang, Lu Yuan, Jenq-Neng Hwang, and Jianfeng Gao. Glipv2: Unifying localization and vision-language understanding. *Advances in Neural Information Processing Systems*, 35:36067–36080, 2022. [2](#), [5](#)
- [41] Xiaoman Zhang, Chaoyi Wu, Ya Zhang, Weidi Xie, and Yanfeng Wang. Knowledge-enhanced visual-language pre-training on chest radiology images. *Nature Communications*, 14(1):4542, 2023. [3](#), [4](#), [5](#), [7](#)
- [42] Yuhao Zhang, Hang Jiang, Yasuhide Miura, Christopher D Manning, and Curtis P Langlotz. Contrastive learning of medical visual representations from paired images and text. *arXiv preprint arXiv:2010.00747*, 2020. [1](#), [2](#), [3](#), [5](#), [6](#), [7](#)
- [43] Chong Zhou, Chen Change Loy, and Bo Dai. Extract free dense labels from clip. In *European Conference on Computer Vision*, pages 696–712. Springer, 2022. [2](#)
- [44] Hong-Yu Zhou, Chenyu Lian, Liansheng Wang, and Yizhou Yu. Advancing radiograph representation learning with masked record modeling. In *The Eleventh International Conference on Learning Representations*, 2023. [2](#), [3](#), [5](#), [7](#)